

Modeling mechanochemical coupling in cell polarity maintenance

Ondrej Maxian

January 3, 2024

Cell polarity is essential for many aspects of organismal development and physiology, including stem cell dynamics, directional cell migration, and asymmetric cell division [6, 10, 12, 18]. On a large scale, a cell’s polarity state is encoded by asymmetric distributions of protein molecules, which are shaped by smaller-scale processes like binding, diffusion, and active transport. The key group of proteins involved in this process are the so-called PAR proteins, which are highly conserved across the metazoa, and are typically distributed asymmetrically during cell division [14, 17] in the presence of actomyosin-mediated contractile flows [21].

The one-cell *C. elegans* embryo is one of the premier model systems for polarization in eukaryotic cells. In this system, polarity is encoded by the distribution of two distinct groups of polarity proteins: anterior PARs (aPARs), which include PAR-3, PAR-6/PKC-3, and CDC-42, and posterior PARs (pPARs), which include PAR-2, PAR-1, LGL-1, and CHIN-1 [17]. Wild-type embryos polarize in two distinct phases termed “establishment” and “maintenance” [3]. In establishment phase, a local sperm cue at the anterior pole acts to load PAR-2 onto the membrane, while at the same time promoting strong anterior-directed actomyosin flows [7]. These cues, together with the mutual inhibition of the aPAR and pPAR domain, sort the PAR proteins into their respective domains, where they are then maintained during maintenance phase [21, 26].

In the language of dynamical systems, it can therefore be said that the *C. elegans* embryo possesses two stable states: a uniform state, in which all of the proteins are distributed symmetrically throughout the cell, and a polarized state, in which the PAR proteins are sorted into their respective domains. The switch between the two states is then governed by the sperm cue, which drives an advective flow to transform the uniform state to the polarized one [9, 11]. Indeed, recent theoretical and experimental studies showed that the cell operates in a regime where cues are necessary to establish polarity, thus avoiding the potentially chaotic case of spontaneous polarization without cues [11].

This analysis suggests that cue-driven flows are required for polarity establishment, and that flow

patterns PAR proteins. Yet, it has been demonstrated repeatedly that embryos lacking a functional flow during establishment phase still polarize, albeit in a delayed manner, and furthermore find the same boundary position as embryos with a functional establishment-phase flow [29, 28]. The flows in these embryos result from a switch from rho-dependent contractility in establishment phase to CDC-42-dependent contractility in maintenance phase [26]. Still though, absent the cue the PAR proteins are the only agents that could pattern actomyosin flows. Thus, these “maintenance-phase” rescue experiments hint that PAR proteins pattern flows, rather than the other way around. This gets at the general question: what are the design principles by which cells combine the PAR protein circuit with actomyosin to robustly encode a dynamically stable polarity state with a fixed boundary position?

Because of the complexity of the *in vivo* system, a definitive answer to this question is only possible with a combination of experiments and modeling. This fact was recognized early on in the field, and indeed there is no dearth of models in the literature (see [27, 5, 4, 8, 11, 9, 15] for a subset). In early models, *potential* mechanics for polarization were explored, but the relative abundance of experimental data in the last decade can allow us to be more precise. For example, an early model of Tostevin and Howard showed that polarity sorting could occur if actomyosin flows feedback onto the aPAR [27] but not pPAR distribution, but recent experiments have shown that both cortical aPARs and pPARs are transported by myosin [13]. We do not take the harsh view that these early models are incorrect; rather, we view them as missing some fundamental biochemistry that was at the time unknown. Consequently, our goal here is to construct a minimal model based on existing experimental evidence that shows how the combination of aPAR/pPAR mutual inhibition and actomyosin flows generate a stable polarity state with fixed boundary position.

Still working on this introductory part. Once we set up a bistable reaction system, the question becomes how we can move from the uniform to the polarized state. Experiments suggest that there are two intrinsic boundary positions here: one (at about 75% egg length) that occurs in the absence of actomyosin flows, and another (at about 50% egg length) that occurs with actomyosin flows [29]. The second case suggests that flows alter the flux balance between the anterior and posterior domains, thus shifting the boundary positions. Indeed, there is a steady state nonzero flow profile observed during maintenance phase, corresponding to an asymmetry in myosin intensity across the A/P boundary [25].

Two questions arise when we consider this data: first, how is the myosin asymmetry maintained without cues? Second, what “brakes” the contractility, i.e., what stops the anterior cap

from contracting off the end of the embryo? The first question can be answered again through experiments and modeling, which have shown that PAR proteins feedback onto myosin dynamics [11, 1]. It remains unclear whether this occurs through pPARs inhibiting myosin (as suggested by [1]) or aPARs recruiting myosin (or inhibiting its dissociation, as suggested in [11]). Modeling work has shown that pPARs *must* inhibit myosin to propagate initially asymmetric protein distributions [15]. Seeing as this hypothesis has been supported experimentally [21, 1], it is the one we use in this work.

Once we set up dynamics in which aPARs and pPARs are mutually bistable, and pPARs inhibit myosin, it is straightforward to see how maintenance phase “rescue” could occur, as the already expanding pPAR domain is then further extended by flow caused from inhibited myosin. But how could this process stop? Previous work [9] proposes a “pinning” of the boundary [20] based on cytoplasmic depletion of PAR-2. As the PAR-2 domain expands, the amount available in the cytoplasm decreases. This changes the local binding/unbinding equilibrium, leading to relative depletion of PAR-2 in the posterior. This levels off myosin inhibition levels, which prevents the build up of strong flows, stalling the boundary.

We propose that this mechanism, while theoretically possible and reproducible in our model, is not the one primarily responsible for stalling the boundary movement. Instead, we postulate that branched actin acts to inhibit contractility in the anterior domain, which prevents myosin from building up and generating stronger flows. We demonstrate **one of these two things**:

1. The hypercontractile state is stable. We can pin it down with the PAR-2 wave-pinning mechanism. The model predicts decreasing PAR-2 on the posterior in this case, which is supported by our experiments.
2. The hypercontractile state is not stable. While we can reproduce it in the model, there is no way to reconcile the parameters we need to reproduce it with the parameters we need to reproduce the wild-type.

Finally, we use modeling to show that branched actin-mediated inhibition of myosin leads to the experimentally-observed myosin and flow profiles, thus validating our hypothesis.

In Section 1, we first rule out the hypothesis that maintenance-phase rescue is driven by spontaneous polarization of myosin, as the flows generated are simply too small to spontaneously polarize the embryo (similar to observations made in establishment phase [22]). We therefore need to incorporate biochemistry to guide the dynamics of myosin. In previous work by some of us [16], we

showed that the maintenance-phase dynamics of PAR-3 are bistable even in the absence of the posterior inhibitor PAR-1. Because of this, it is our hypothesis that PAR-3 provides an anchor for the bistability of the entire system. We utilize this hypothesis in Section 2, where we set up a model describing the maintenance phase biochemistry. While this model is capable of amplifying small asymmetries to produce polarized states, the timescale on which this occurs is roughly ten times larger than the duration of maintenance phase, indicating the need for contractility to speed up the process. Therefore, in Section 3, we demonstrate how combining our biochemistry and contractility models can reproduce maintenance-phase experimental observations.

1 Maintenance-phase myosin dynamics

Movies of the maintenance phase rescue process make it appear as though the system spontaneously breaks symmetry. With that in mind, we explore a possible mechanism whereby the dynamics of myosin could be intrinsically unstable, and those dynamics could generate flows which pattern the PAR proteins. To do this, we first consider a model of myosin by itself, similar to what has already been considered in [2].

We describe the dynamics of myosin $M(x, t)$ using the advection-diffusion-reaction equations

$$\partial_t M + \partial_x (vM) = D_M \partial_x^2 M + k_M^{\text{on}} M_{\text{cyto}} - k_M^{\text{off}} M \quad (1a)$$

$$\gamma v = \eta \partial_x^2 v + \partial_x \sigma_a(M) \quad (1b)$$

$$M_{\text{cyto}} = \frac{1}{hL} \left(M^{(\text{Tot})} L - \int_0^L M(x) dx \right) \quad (1c)$$

The velocity field (1b) comes from the assumption that myosin generates an active stress $\sigma_a(M)$, which combines with the viscous stress to give the total cortical stress

$$\sigma = \eta \partial_x v + \sigma_a(M). \quad (2)$$

As in [2], we ignore the elastic part of the stress, since the actomyosin cortex is purely viscous on timescales longer than the cortical turnover time [19]. The force balance equation in the fluid says that the force due to stress must be balanced by the drag force,

$$\gamma v = \partial_x \sigma, \quad (3)$$

where γ is the drag coefficient. Combining the force balance (3) with the stress expression (2) gives (1b).

Parameter	Description	Value	Units	Ref	Notes
L	Domain length	134.6	μm	[9]	radii $27 \times 15 \mu\text{m}$ ellipse
h	Cytoplasmic “thickness”	9.5	μm	[9]	(area/circumference)
D_M	Myosin diffusivity	0.05	$\mu\text{m}^2/\text{s}$	[11]	Fit to get 30% bound myosin
k_M^{on}	Myosin attachment rate	0.5	$\mu\text{m}/\text{s}$	[11]	
k_M^{off}	Myosin detachment rate	0.12	1/s		
$M^{(\text{Tot})}$	Maximum bound myosin density	–	$\#/\mu\text{m}$		Scales out of equations
η	Cytoskeletal fluid viscosity	0.1	Pa·s		$100 \times \text{water}$
γ	Myosin drag coefficient	10^{-3}	Pa·s/ μm^2		$\ell = \sqrt{\eta/\gamma} = 10 \mu\text{m}$ [24]
σ_0	Stress coefficient and form	0.0042	Pa		Fit in Sec. 1.1.1
$\hat{\sigma}_a(\hat{M})$	Stress function of myosin	\hat{M}			Fit in Sec. 1.1.1

Table 1: Parameter values for myosin model. All of these parameters listed with a citation are lifted directly from the corresponding paper. Remaining parameters: the on rate k_M^{on} is chosen to give 30% bound myosin [11, Fig. S3]. Later this rate will change in the presence of CDC-42. We make an assumption about the fluid viscosity η , which then gives us the drag coefficient γ from $\ell = 10 \mu\text{m}$ [11]. The remaining parameters are fit in Section 1.1.1 from the wild-type data of [25].

It will be useful to nondimensionalize the system (1), using the scalings

$$x = \hat{x}L \quad t = \hat{t}/k_M^{\text{off}} \quad M = \hat{M}M^{(\text{Tot})} \quad v = \hat{v} \frac{\sigma_0}{\sqrt{\eta\gamma}}, \quad (4)$$

where L is the embryo perimeter and $M^{(\text{Tot})}$ is the concentration of myosin if it were all uniformly bound to the membrane. The resulting equations are

$$\partial_{\hat{t}}\hat{M} + \hat{\sigma}_0\partial_{\hat{x}}(\hat{v}\hat{M}) = \hat{D}_M\partial_{\hat{x}}^2\hat{M} + \hat{K}_M^{\text{on}}\left(1 - \int_0^1 \hat{M}(x) dx\right) - \hat{M} \quad (5a)$$

$$\hat{v} = \hat{\ell}^2\partial_{\hat{x}}^2\hat{v} + \hat{\ell}\partial_{\hat{x}}\hat{\sigma}_a(\hat{M}) \quad (5b)$$

and are controlled by the dimensionless parameters

$$\hat{\sigma}_0 = \left(\frac{\sigma_0/\sqrt{\eta\gamma}}{Lk_M^{\text{off}}}\right) \quad \hat{D}_M = \frac{D_M}{k_M^{\text{off}}L^2} \quad \hat{K}_M^{\text{on}} = \frac{k_M^{\text{on}}}{hk_M^{\text{off}}} \quad \hat{\ell} = \frac{\sqrt{\eta/\gamma}}{L}. \quad (6)$$

Recalling that $1/k_M^{\text{off}}$ is the residence time, these dimensionless parameters can be understood in the following way:

1. $\hat{\sigma}_0$ is the fraction of the domain that active transport occurs on before a myosin molecule jumps off. To see this, note that residence time \times the advective velocity $\sigma_0/\sqrt{\eta\gamma}$ is the amount of motion, which is normalized by the domain length.

2. \hat{D}_M is the maximum fraction of the domain a molecule diffuses before it unbinds (in the extreme case when the gradient in the domain is $1/L$, the diffusive velocity is D_M/L).
3. \hat{K}_M^{on} sets the uniform steady state of the model by $\hat{M}_0 = \hat{K}_M^{\text{on}} / (1 + \hat{K}_M^{\text{on}})$.
4. $\hat{\ell}$ is the ratio of the hydrodynamic lengthscale (the lengthscale on which fluid flows can “grab” neighboring molecules) to the domain length.

Prior to performing linear stability analysis, we need to first determine the function σ_a and the other parameters. We do this in the next section by fitting experimental data.

1.1 Parameter estimation

Table 1 lists the parameters for the myosin model. According to [9], the *C. elegans* embryo has a roughly ellipsoidal shape, with half-axis lengths $27 \times 15 \times 15 \mu\text{m}$. As such, our model will be a 27×15 ellipse, which has perimeter $L = 134.6 \mu\text{m}$. In our one-dimensional model, the cytoplasm has a “thickness” which is just the area of the ellipse $1272 \mu\text{m}^2$ divided by the perimeter L , which gives $h = 9.5 \mu\text{m}$.

The next category of parameters relates to the myosin kinetics. The in-membrane diffusivity of myosin, as well as the detachment rate, have both been measured in [11]. For the attachment rate, it was estimated in [11, Fig. S3m] that roughly 30% of myosin is bound to the cortex in wild-type embryos. Recalling that the uniform steady state is $\hat{M}_0 = \hat{K}_M^{\text{on}} / (1 + \hat{K}_M^{\text{on}})$, this gives $\hat{K}_M^{\text{on}} = 0.43$, or $k_M^{\text{on}} = 0.43hk_M^{\text{off}} = 0.5 \mu\text{m/s}$. The last parameter, the total amount of myosin, scales out of the equations. This is fortunate for us because it is difficult to think about a total amount over a cross-section.

For the fluid parameters, we assume that the viscosity of the cytoskeletal fluid on the cortex is 100 times water, which gives $0.1 \text{ Pa}\cdot\text{s}$. The “hydrodynamic length scale” of $\ell = \sqrt{\eta/\gamma} = 10 \mu\text{m}$, measured in [19, 24], then gives the myosin drag coefficient γ . But more important than either of these is the stress as a function of myosin concentration. We fit this from the wild-type data of [25] in the next section.

1.1.1 Inferring flow profile from experiments

Because we can measure the cortical velocity and myosin intensity, we can actually infer the function $\sigma_a(M)$ in dimensional units from the experimental data [25]. We in particular isolate the myosin intensity and flow speed during “late maintenance” phase in wild type embryos [25, Fig. 1B(bottom)],

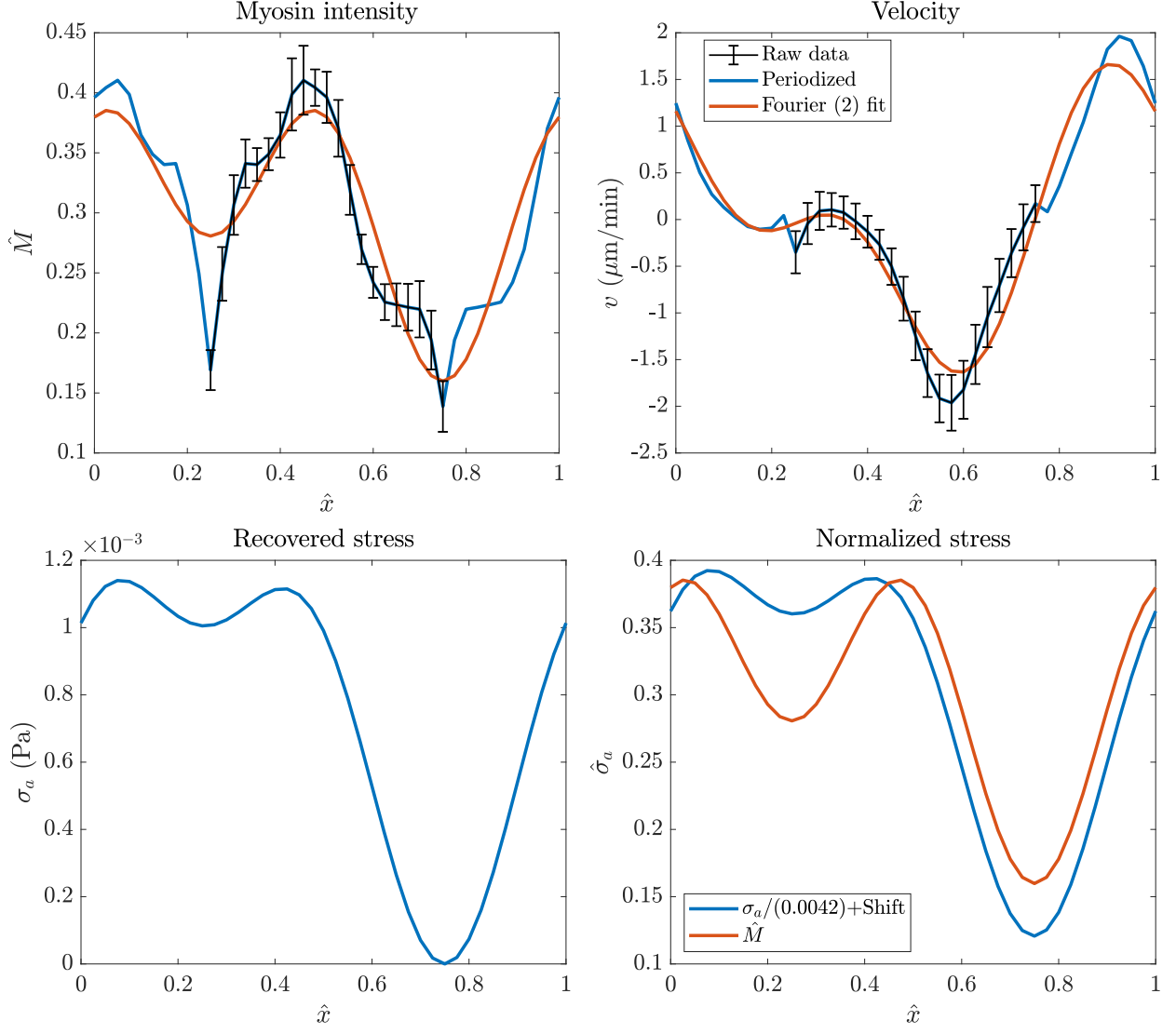


Figure 1: Extracting the velocity profile and active stress from wild-type embryos. Top: the experimental data for myosin intensity (left) and velocity in $\mu\text{m}/\text{min}$ (right). We show the raw data in black (which goes from anterior to posterior), the periodized version in blue, and a two-term (three terms if we include the constant) Fourier series representation in red. Bottom left: the recovered stress profile $\sigma_a(\hat{x})$ in dimensional units. Bottom right: comparing the recovered stress to the myosin intensity, after normalizing by $\sigma_0 = 0.0042$ Pa. It is clear that $\hat{\sigma}_a = \hat{M}$ is a reasonable approximation.

plotting the results in the top panels of Fig. 1. In the top left plot, we plot the myosin intensity, normalized so that the mean amount of bound myosin is 0.3, in accordance with wild-type measurements in [11, Fig. S3].

In the top right plot, we show the velocity in $\mu\text{m}/\text{min}$. In both cases, the data are plotted on $\hat{x} \in [0.25, 0.75]$, which corresponds to half of the embryo (one of the lines going from anterior to posterior end). We then periodically extend this data so that we fill the whole circumference $\hat{x} \in [0, 1]$; these are the blue lines in Fig. 1. Finally, to remove the noise from our measurements (e.g., the strange dips in the myosin concentration at the anteior and posterior pole), we fit the periodized version with a two-term (+constant) Fourier representation, which gives the red lines in Fig. 1.

To extract the stress profile from the smoothed velocity and myosin intensity, we consider a hybrid dimensional form of (1b)

$$\gamma v - \frac{\eta}{L^2} \partial_{\hat{x}}^2 v = \frac{1}{L} \partial_{\hat{x}} \sigma_a(M).$$

Let the Fourier series representation for $v(\hat{x}) = \sum_k \tilde{v}(k) \exp(2\pi i k \hat{x})$, and likewise for $\hat{\sigma}_a$. Then, in Fourier space, the solution for σ_a is given by

$$\sigma_a(k) = \frac{\gamma + \eta/L^2 (2\pi k)^2}{2\pi i k/L} \tilde{v}(k). \quad (7)$$

The $k = 0$ mode is undefined because σ_a only appears differentiated; we therefore set it such that the real space stress has a minimum value of zero.

We plug the parameters from Table 1 into (7) and show the resulting real space stress in the bottom left panel of Fig. 1. This is the dimensional stress σ_a . In the right panel of Fig. 1, we normalize and shift the stress so that it has the same mean and range as the myosin profile \hat{M} . Obtaining the same range allows us to read off the constant $\sigma_0 = 4.2 \times 10^{-3}$ Pa that controls the magnitude of the advective flows. In particular, the dimensionless parameter $\hat{\sigma}_0$ defined in (6) is seen to be equal to

$$\hat{\sigma}_0 = \left(\frac{\sigma_0 / \sqrt{\eta \gamma}}{L k_M^{\text{off}}} \right) = 0.026. \quad (8)$$

In addition, the bottom right panel of Fig. 1, also shows that we can roughly set

$$\hat{\sigma}_a = \hat{M} \quad (9)$$

as a good approximation to the stress. The function itself is ambiguous, since $\hat{M} = 0.3$ defines two different values of the stress depending on the side of the domain, but $\hat{\sigma}_a = \hat{M}$ appears to be a good approximation.

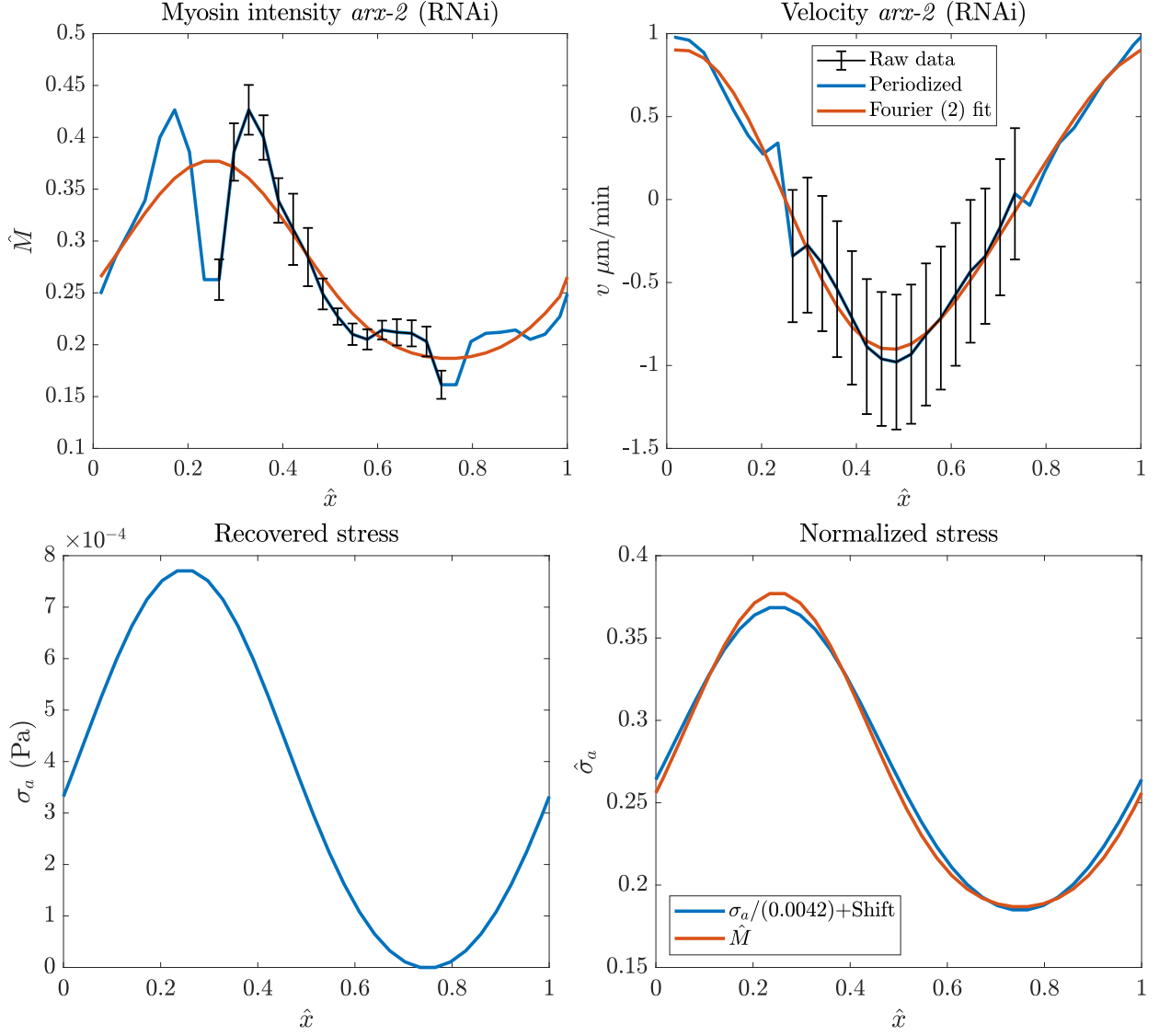


Figure 2: Same plot as Fig. 1, but in *arx-2* (RNAi) embryos. In the bottom right plot, we normalize by $\sigma_0 = 4.2 \times 10^{-3}$ Pa. This makes the stress (when shifted by an arbitrary constant) roughly the same as the myosin profile (also normalized so its maximum is 1).

We confirm this in Fig. 2, where we repeat the velocity fitting procedure in *arx-2* (RNAi) embryos, which lack branched actin and consequently have a simpler velocity profile. To compute the myosin profile, we assume that the experimentally-measured intensity can be converted to the dimensionless concentration \hat{M} via the same factor (0.21) as wild-type embryos. Consequently, the myosin profile we obtain is in the top left of Fig. 2. The velocity is shown in the top right panel, and we extract the stress profile in the bottom left in exactly the same way as in wild-type. Then, to compute normalized stress we divide out by $\hat{\sigma}_0 = 4.2 \times 10^{-3}$ Pa (obtained from wild-type). The normalized stress, when shifted by an arbitrary constant, lines up almost perfectly with the smoothed myosin profile, demonstrating that our rough approach from wild-type embryos extends to other embryos as well. Thus, this section gives us $\sigma_a = (4.2 \times 10^{-3}) \hat{M}$.

1.2 Linear stability analysis

Now that all the parameters are known, we can perform linear stability analysis to see if the system could spontaneously polarize. The uniform steady state is $\hat{M}_0 = \hat{K}_M^{\text{on}} / (1 + \hat{K}_M^{\text{on}})$. We consider a perturbation around that state $\hat{M} = \hat{M}_0 + \delta\hat{M}$, where $\delta\hat{M} = \delta\hat{M}_0 e^{\lambda(k)\hat{\ell} + 2\pi i k \hat{x}}$. Plugging this into (5b), we get the velocity [2, Eq. (11)]

$$\hat{v} = \frac{2\pi i k \hat{\ell} \hat{\sigma}'_a(\hat{M}_0)}{1 + (2\pi k \hat{\ell})^2} \delta\hat{M}. \quad (10)$$

Substituting this velocity into (5a), and considering only the first order terms, we get the following equation for the eigenvalues

$$\lambda(k) = \frac{4\pi^2 k^2 \hat{\ell} \hat{M}_0 \hat{\sigma}_0 \hat{\sigma}'_a(\hat{M}_0)}{1 + 4\pi^2 k^2 \hat{\ell}^2} - \hat{D}_M 4\pi^2 k^2 - 1 \quad (11)$$

Using the parameters we have obtained, we have the following values for the dimensionless groups

$$\hat{D}_M = 2.3 \times 10^{-5} \quad \hat{M}_0 \approx 0.3 \quad \hat{\sigma}'_a = 1 \quad \hat{\ell} \approx 0.07 \quad (12)$$

This gives the dispersion relation shown in Fig. 3 for different values of $\hat{\sigma}_0$. We observe strong flow coupling required for instability; with $\hat{\sigma}_0 = 0.2$ (flow transports myosins around 20% of the cell before they come off), we still do not see any instability. Considering that we already have seen wild-type embryos have $\hat{\sigma}_0 \approx 0.03$, it is clear that myosin cannot self-polarize in the zygote.

Importantly, the large value of $\hat{\sigma}_0$ needed for instability is a consequence of the -1 in the dispersion relation (11), which comes from the unbinding kinetics. Thus, unbinding makes it *harder* to destabilize the uniform steady state. Indeed, without the -1 , the instability occurs at $\hat{\sigma}_0 \approx 10^{-3}$,

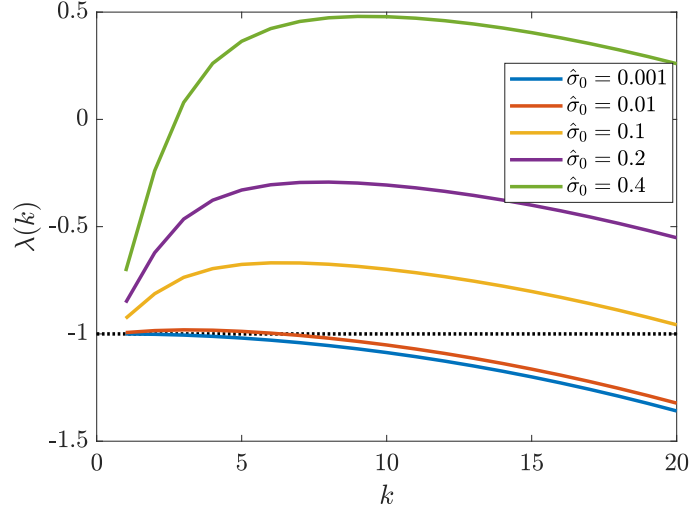


Figure 3: Dispersion relation (11) for myosin for different values of $\hat{\sigma}_0$. Positive eigenvalues indicate instability of the steady state. Dotted black line at $\lambda = -1$ reflects the axis of instability *without* unbinding kinetics.

which is pretty weak coupling to the flow (and weaker coupling than we observe experimentally). When we account for unbinding, diffusion becomes so small as to be irrelevant, as for the $k = 1$ mode the coefficient in (11) is $\hat{D}_M 4\pi^2 \approx 10^{-3}$. **Thus, the real balance here (to generate the instability) is not between advection and diffusion, but between advection and *unbinding*.** Specifically, the advective flow must be strong enough to overcome the increase in unbinding that happens in areas enriched in myosin. Our data clearly demonstrate that this does not occur in maintenance phase, making the dynamics of myosin by itself stable to perturbations. This means that maintenance-phase rescue must be a result of PAR proteins signaling myosin. The next section lays out our model of the maintenance phase PAR protein circuit that we use for this purpose.

2 Maintenance phase biochemistry

Our biochemistry model is based on the diagram shown in Fig. 4, which in turn comes from [17, Fig. 2]. On the anterior side, we have three distinct protein species: PAR-3 (A), which has intrinsically bistable dynamics as a result of oligomerization and positive feedback [16], CDC-42 (C), which is necessary for communication with myosin, and PAR-6/PKC-3 (K), which inhibits the posterior PARs. Unlike the anterior PARs, which each have their own independent function,

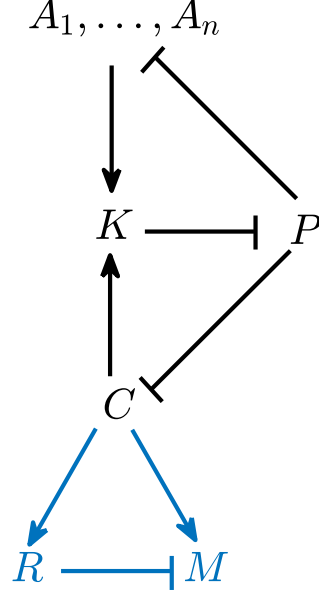


Figure 4: Schematic of the biochemistry model. We consider the black parts (biochemistry only) in Section 2, and add the blue parts (contractility) in Section 3. On the anterior half, A represents PAR-3 (in monomer and oligomer form), K represents the PAR-6/PKC-3 complex, and C represents CDC-42. The posterior PARs can be represented by a single protein species P .

the posterior PARs (PAR-2, PAR-1, and CHIN-1) can be lumped into one species (denoted by P), which antagonizes both PAR-3 (by inhibiting oligomerization) and CDC-42.

We have already studied the dynamics of PAR-3 without its posterior inhibitor in previous work [16]. In the absence of posterior inhibition, the oligomerization equilibrium is given by $k_A^{\text{dp}} A_n = k_A^{\text{p}} A_{n-1} A_1$, where k_A^{dp} is the depolymerization rate, k_A^{p} is the polymerization rate, and A_n is the concentration of oligomer size n . We convert to dimensionless variables by setting $\hat{A} = A/A^{(\text{Tot})}$, where $A^{(\text{Tot})}$ is the (unknown) total amount of PAR-3 in the system. This gives the oligomerization equilibrium $\hat{A}_n = \hat{K}_A^{\text{p}} \hat{A}_{n-1} \hat{A}_1$, where $\hat{K}_A^{\text{p}} = A^{(\text{Tot})} k_A^{\text{p}} / k_A^{\text{dp}}$ is the dimensionless polymerization rate. To account for the inhibition of PAR-3 cluster growth by PAR-1 (P), we increase the effective depolymerization rate by setting

$$\hat{K}_{\text{AP}}^{\text{p}}(\hat{P}) = \frac{k_A^{\text{p}} A^{(\text{Tot})}}{k_A^{\text{dp}} (1 + \hat{R}_{\text{PA}} \hat{P})} = \frac{\hat{K}_A^{\text{p}}}{1 + \hat{R}_{\text{PA}} \hat{P}} \quad (13)$$

where $\hat{R}_{\text{PA}} = r_{\text{PA}} P^{(\text{Tot})} / k_A^{\text{dp}}$ describes the rate at which pPARs inhibit cluster accumulation relative to the normal rate of depolymerization k_A^{dp} .

PAR-3 also gates the association of CDC-42 with PAR-6/PKC-3 (K), which is a complex that inhibits all posterior PARs. To model this, we work off the observations in [25], which reveal

that PAR-6/PKC-3 are recruited to the membrane by CDC-42, provided that there is a sufficient concentration (roughly 10% of the enriched anterior level) of PAR-3 on the membrane. Absent PAR-3, there is no loading of PAR-6/PKC-3 onto the membrane, so we have no basal rate of loading, and the total loading term is proportional to the CDC-42 concentration times the cytoplasmic concentration of K , provided the PAR-3 concentration satisfies $\hat{A} > \hat{A}_0$. That is, the on rate for \hat{K} is equal to $\hat{C}\delta_{\hat{A} > \hat{A}_0}\hat{K}_{\text{cyto}}$, where $\delta_{\hat{A} > \hat{A}_0}(\hat{x})$ is 1 if $\hat{A}(\hat{x}) > \hat{A}_0(\hat{x})$ and 0 otherwise.

With these preliminaries, we can now formulate the full dimensionless set of reaction-diffusion equations that describe the interactions in Fig. 4

$$\partial_t \hat{A}_1 = \hat{D}_A \partial_x^2 \hat{A}_1 + \hat{K}_A^{\text{on}} \left(1 + \hat{K}_A^{\text{f}} \hat{F}_A(\hat{A})\right) \left(1 - \int_0^1 \hat{A}(x) d\hat{x}\right) - \hat{K}_A^{\text{off}} \hat{A}_1 \quad (14a)$$

$$+ 2\hat{A}_2 - 2\hat{K}_{\text{AP}}^{\text{p}} \hat{A}_1^2 + \sum_{n=3}^N \left(\hat{A}_n - \hat{K}_{\text{AP}}^{\text{p}} \hat{A}_1 \hat{A}_{n-1}\right) \quad (14b)$$

$$\partial_t \hat{A}_n = \hat{K}_{\text{AP}}^{\text{p}} \hat{A}_1 (\hat{A}_{n-1} - \hat{A}_n) - (\hat{A}_n - \hat{A}_{n+1}) \quad N > n \geq 2 \quad (14c)$$

$$\partial_t \hat{A}_N = \hat{K}_{\text{AP}}^{\text{p}} \hat{A}_1 \hat{A}_{N-1} - \hat{A}_N \quad (14d)$$

$$\partial_t \hat{C} = \hat{D}_C \partial_x^2 \hat{C} + \hat{K}_C^{\text{on}} \left(1 - \int_0^1 \hat{C}(\hat{x}) d\hat{x}\right) - \hat{K}_C^{\text{off}} (1 + \hat{R}_{\text{PC}} \hat{P}) \hat{C} \quad (14e)$$

$$\partial_t \hat{K} = \hat{D}_K \partial_x^2 \hat{K} + \hat{R}_{\text{ACK}} \hat{C} \delta_{\hat{A} > \hat{A}_0} \left(1 - \int_0^1 \hat{K}(\hat{x}) d\hat{x}\right) - \hat{K}_K^{\text{off}} \hat{K} \quad (14f)$$

$$\partial_t \hat{P} = \hat{D}_P \partial_x^2 \hat{P} + \hat{K}_P^{\text{on}} \left(1 - \int_0^1 \hat{P}(\hat{x}) d\hat{x}\right) - \hat{K}_P^{\text{off}} (1 + \hat{R}_{\text{KP}} \hat{K}) \hat{P} \quad (14g)$$

The first two equations describe the dynamics of PAR-3, and are unchanged from [16] with the exception that the dimensionless polymerization rate is now a function of \hat{P} . The other three equations describe, respectively, the dynamics of CDC-42 (C), PAR-6/PKC-3 (K), and all posterior PARs (P).

2.1 Parameters

The first set of parameters for the model (14) have to do with the intrinsic PAR-3 dynamics. In dimensionless form, they are

$$\hat{D}_A = \frac{D_A}{L^2 k_A^{\text{dp}}}, \quad \hat{K}_A^{\text{on}} = \frac{k_A^{\text{on}}}{k_A^{\text{dp}} h}, \quad \hat{K}_A^{\text{f}} = \frac{k_A^+ A^{(\text{Tot})}}{k_A^{\text{on}}}, \quad \hat{K}_A^{\text{off}} = \frac{k_A^{\text{off}}}{k_A^{\text{dp}}}, \quad \hat{K}_A^{\text{p}} = \frac{k_A^{\text{p}} A^{(\text{Tot})}}{k_A^{\text{dp}}}.$$

All of these parameters have been either experimentally measured or fit in [16]. The values we use are in Table 2. For the feedback function we use a saturated linear feedback $\hat{F}(\hat{A}) = \min(\hat{A}, \hat{A}^{(\text{Sat})})$, where the saturation threshold is chosen at 80% of the uniform steady state to ensure its stability. See [16] for more details on this.

Parameter	Description	Value	Units
L	Domain length	134.6	μm
h	Cytoplasmic “thickness”	9.5	μm
D_A	Monomeric PAR-3 diffusivity	0.1	$\mu\text{m}^2/\text{s}$
k_A^{on}	Monomeric PAR-3 attachment rate	1	$\mu\text{m}/\text{s}$
k_A^{off}	Monomeric PAR-3 detachment rate	3	1/s
k_A^{dp}	PAR-3 depolymerization rate	0.16	1/s
\hat{K}_A^{p}	PAR-3 polymerization rate	15	
\hat{K}_A^{f}	PAR-3 self recruitment rate	3.6	
N	Max oligomer size	50	

Table 2: Parameter values for the PAR-3 model. All of these parameters come from [16].

Parameter	Description	Value	Units	Ref	Notes
D_P	pPAR diffusivity	0.15	$\mu\text{m}^2/\text{s}$	[9]	Same as PAR-6
D_K	PAR-6 diffusivity	0.1	$\mu\text{m}^2/\text{s}$	[23]	
D_C	CDC-42 diffusivity	0.1	$\mu\text{m}^2/\text{s}$		
k_P^{off}	pPAR detachment rate	7.3×10^{-3}	1/s	[9]	
k_K^{off}	PAR-6 detachment rate	0.01	1/s	[23]	
k_C^{off}	CDC-42 detachment rate	0.01	1/s		
k_P^{on}	PAR-2 attachment rate	0.13	$\mu\text{m}/\text{s}$	[11]	$P \approx 1$ in enrichment zone
\hat{R}_{KP}	K inhibiting P	50			Strong inhibition
\hat{R}_{PC}	P inhibiting C	(17)		[25]	CDC/CHIN-1 relationship (Fig. A5)
k_C^{on}	CDC-42 attachment rate	0.1	$\mu\text{m}/\text{s}$		20% bound with inhibition
\hat{A}_0	PAR-3 threshold for PAR-6	0.06		[25]	10% anterior level
\hat{R}_{ACK}	A and C creating K	0.1			20% bound K
\hat{R}_{PA}	P inhibiting A	2			α on posterior in wild-type

Table 3: Additional parameter values for the biochemistry model.

The other dimensionless parameters that appear in (14) are

$$\hat{R}_{PA} = \frac{r_{PA}P^{(\text{Tot})}}{k_A^{\text{dp}}}, \quad \hat{R}_{PC} = \frac{r_{PC}P^{(\text{Tot})}}{k_C^{\text{off}}}, \quad \hat{R}_{ACK} = \frac{r_{ACK}C^{(\text{Tot})}}{k_A^{\text{dp}}h}, \quad \hat{R}_{KP} = \frac{r_{KP}K^{(\text{Tot})}}{k_P^{\text{off}}} \quad (15a)$$

$$\hat{K}_P^{\text{on}} = \frac{k_P^{\text{on}}}{k_A^{\text{dp}}h}, \quad \hat{K}_C^{\text{on}} = \frac{k_C^{\text{on}}}{k_A^{\text{dp}}h}, \quad \hat{A}_0 = \frac{A_0}{A^{(\text{Tot})}} \quad (15b)$$

$$\hat{D}_P = \frac{D_P}{L^2 k_A^{\text{dp}}}, \quad \hat{D}_C = \frac{D_C}{L^2 k_A^{\text{dp}}}, \quad \hat{D}_K = \frac{D_K}{L^2 k_A^{\text{dp}}}, \quad \hat{K}_P^{\text{off}} = \frac{k_P^{\text{off}}}{k_A^{\text{dp}}}, \quad \hat{K}_K^{\text{off}} = \frac{k_K^{\text{off}}}{k_A^{\text{dp}}}, \quad \hat{K}_C^{\text{off}} = \frac{k_C^{\text{off}}}{k_A^{\text{dp}}} \quad (15c)$$

Among these, the parameters in (15c) are all known from literature, and have been reported in the top half of Table 3. This leaves the seven parameters in (15a) and (15b), which we determine sequentially from the following set of experimental observations:

1. In embryos without myosin flows, roughly 25–30% of the available PAR-2 is bound at steady state [11, Fig. S3]. Because the PAR-2 domain is only 25–30% of the embryo, the concentration of P in its enrichment zone must be near 1. We find that $k_P^{\text{on}} = 0.13 \mu\text{m/s}$, which is the value obtained from fitting in [11], reproduces this result.
2. In embryos without myosin flows, the level of PAR-2 at the anterior is no more than 5% of the posterior level [11, Fig. 2c]. This sets $\hat{R}_{KP} \gg 1$. We use $\hat{R}_{KP} = 50$ for strong inhibition.
3. The parameter \hat{R}_{PC} is available from the data in [25]. To obtain it, we solve (14e) at steady state to obtain

$$\hat{C} = \frac{1}{1 + \frac{hk_c^{\text{off}}}{k_C^{\text{on}}} + \frac{\hat{R}_{PC}k_C^{\text{off}}h}{k_C^{\text{on}}}\hat{P}}. \quad (16)$$

Now according to [25], in a system of units where $\hat{C} = 1$ when $\hat{P} = 0$,

$$\tilde{C} = \frac{1 + \frac{hk_c^{\text{off}}}{k_C^{\text{on}}}}{1 + \frac{hk_c^{\text{off}}}{k_C^{\text{on}}} + \frac{\hat{R}_{PC}k_C^{\text{off}}h}{k_C^{\text{on}}}\hat{P}}$$

we have $\tilde{C} \approx 1/(1 + 13.3\hat{P})$, which implies that

$$13.3 = \frac{\hat{R}_{PC}k_C^{\text{off}}h}{k_C^{\text{on}} \left(1 + \frac{hk_c^{\text{off}}}{k_C^{\text{on}}}\right)} = \frac{\hat{R}_{PC}k_C^{\text{off}}h}{k_C^{\text{on}} + hk_c^{\text{off}}} \rightarrow \hat{R}_{PC} = 13.3 \left(1 + \frac{k_C^{\text{on}}}{k_C^{\text{off}}h}\right). \quad (17)$$

4. In [11, Fig. S3i], it is reported that roughly 25% of PAR-6 is bound in wild-type embryos. Assuming that CDC-42 has a similar set of properties, we can assume 25% of the protein is bound. Setting $k_C^{\text{on}} = 0.1 \mu\text{m/s}$ and combining with the inhibition strength (17) gives about 20% bound CDC-42 at steady state.

5. Let's assume $\hat{C} = 0.25$; then we want to set \hat{R}_{ACK} to obtain about 25% bound PAR-6 (when there is sufficient PAR-3) as well. Plugging this into the steady state version of (14f), we obtain

$$\hat{R}_{\text{ACK}}(0.25)(0.75) - (0.0625)(0.25) = 0 \rightarrow \hat{R}_{\text{ACK}} = 0.08 \approx 0.1.$$

6. In embryos depleted of PAR-1 and CHIN-1, the level of PAR-3 at the anterior is roughly 10% of the posterior, and PAR-6 can load onto the membrane everywhere. We therefore set $\hat{A}_0 = 0.06$, since we've already tuned the PAR-3 parameters so that the polarized state has $\hat{A} \approx 0.6$ on the anterior and $\hat{A} \approx 0.06$ on the posterior [16].

We will for the moment leave the parameter \hat{R}_{PA} unset, and look at how the model changes when we vary it. The way the rest of parameters are set is summarized in Table 3.

2.2 How inhibition of PAR-3 oligomerization dictates behavior

We now try to understand how the biochemistry model (14) can behave for different choices of the PAR-1/PAR-3 inhibition strength \hat{R}_{PA} . To accomplish this, we set up an initial condition shown in the top left of Fig. 5, where PAR-3 (A) is enriched in the middle 50% of the embryo, while posterior PARs (P) are enriched in the outer 50%. CDC-42 (C) is distributed uniformly, and no PAR-6/PKC-3 (K) is bound to the membrane. We then run the model forward in time until $\hat{t} = 200$ (20 minutes of real time) and look at how the distributions of the proteins evolve.

Based on the results in Fig. 5, we distinguish three different regimes of inhibition:

1. In the regime where \hat{R}_{PA} is small (top right), there is not enough inhibition of PAR-3 to prevent it from accumulating on the posterior at 10% of its anterior level. Because of this, the PAR-6/PKC-3 complex accumulates uniformly on the membrane. Consequently, posterior PARs and CDC-42 all accumulate uniformly (there are still some small residual asymmetries left over from the initial data in the plot).
2. In the regime where \hat{R}_{PA} is large (bottom right), a small amount of pPARs are sufficient to drive PAR-3 down to its smallest value. Thus, the pPARs outcompete PAR-3, which sets up a state where *all* of the proteins are distributed uniformly.
3. For intermediate values of \hat{R}_{PA} (bottom left, the exact range is $1 \lesssim \hat{R}_{\text{PA}} \lesssim 20$), PAR-1 locally drives PAR-3 into its monomer form, which leads to more unbinding. In these regions, the

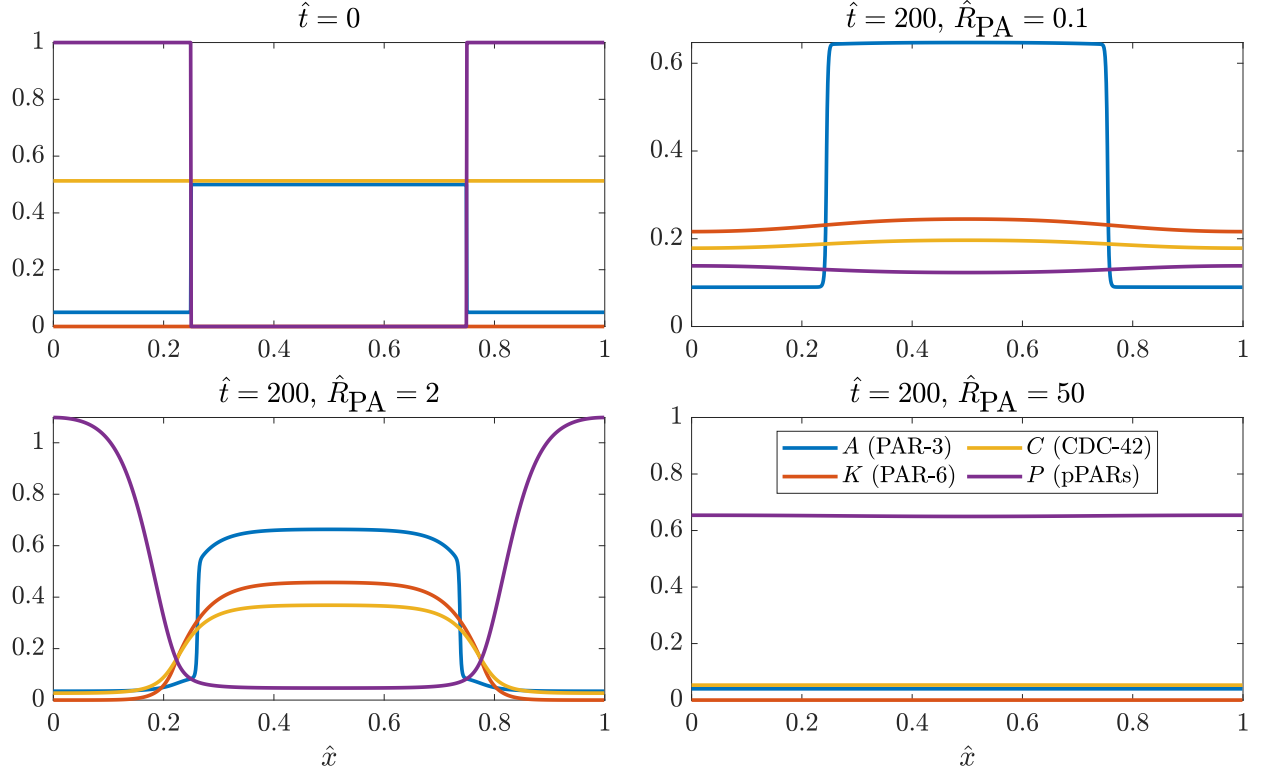


Figure 5: Dynamics of biochemistry model (14) with different strengths of PAR-3 cluster inhibition by PAR-1 (parameter \hat{R}_{PA}). Top left: the initial condition we use for the simulations. PAR-3 (A) is enriched in the middle 50% of the embryo, while posterior PARs (P) are enriched in the outer 10%. CDC-42 (C) is distributed uniformly, and no PAR-6/PKC-3 (K) is bound to the membrane. The next three plots show the state at $\hat{t} = 200$ (about 20 minutes of real time) with three different values of \hat{R}_{PA} .

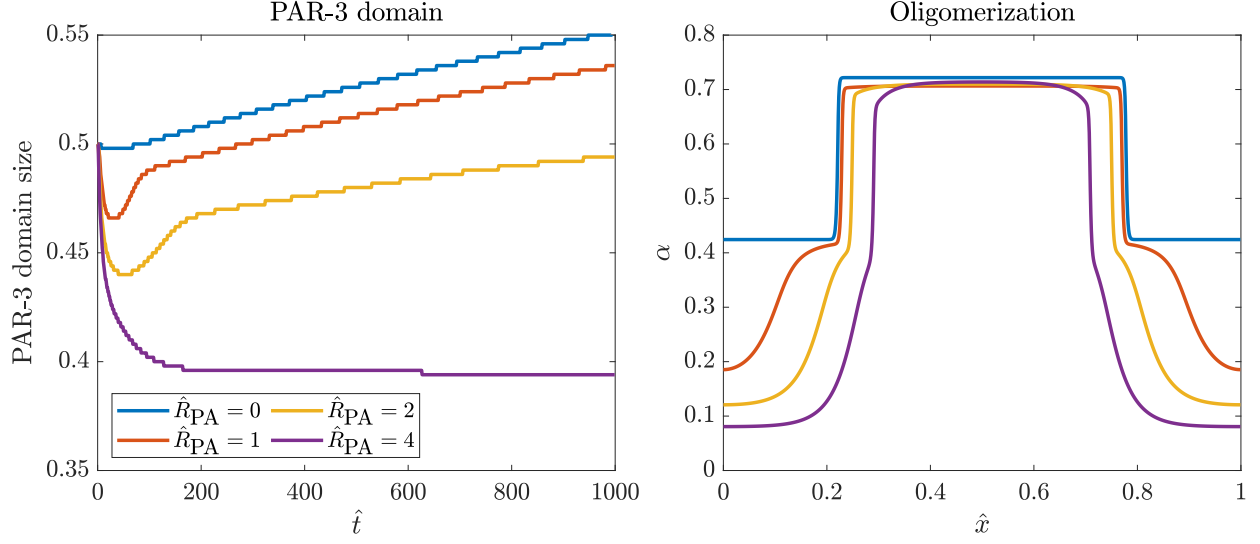


Figure 6: Steady state domain sizes and oligomerization kinetics with biochemistry model (14), varying parameter \hat{R}_{PA} . We show the PAR-3 domain size over time (left) and α values at steady state (right) for three different values of \hat{R}_{PA} .

pPARs outcompete PAR-3 and bind to the membrane, and there is a steady state where PAR-3 and the pPARs are separated by a buffer zone of PAR-6/PKC-3.

Obviously, the wild-type system must fall into the third regime. While this gives a large range of parameters for R_{PA} , if the inhibition is too large then even a small amount of P (as on the anterior) could affect the polymerization dynamics of PAR-3. We want to avoid this regime, and so we set $\hat{R}_{PA} = 2$. With this value, the steady state A/P ratio of PAR-3 goes from about 7:1 without P inhibition to 20:1 with P inhibition, which qualitatively matches the experimental dynamics of a roughly 5 fold change [25, Fig. 4c].

2.2.1 Setting the inhibition strength \hat{R}_{PA} based on steady states

When we operate in the regime where there is stable polarized state (PAR-3 enriched in half the embryo, pPARs enriched in the other half), the parameter \hat{R}_{PA} also affects the distribution of oligomer sizes on the posterior. To determine the value of \hat{R}_{PA} , we simulate to steady state with several different values, and plot the PAR-3 domain size over time and α values at steady state in Fig. 6. To mimic the onset maintenance phase, we start the system in a state where 50% of the domain is enriched in PAR-3, then watch the boundary expand/contract.

When we start the system at the end of establishment phase, we find that the PAR-3 boundary

is quasi-stable when $\hat{R}_{PA} \leq 2$. For $\hat{R} > 2$, there is a shift to a smaller domain size on a timescale of $\hat{t} = 100$ (10 minutes of real time). Because the system is in a quasi-stable state, it is logical to look at the α value on the posterior as a way to constrain the value of \hat{R}_{PA} . Figure 6 shows that $\alpha = 0.42$ without PAR-1 inhibition (30% in monomer form) [16], while when $\hat{R}_{PA} = 1, 2$, and 4 we have $\alpha = 0.19, 0.12$, and 0.08, respectively. These values of α correspond roughly to 65, 75, and 85% in monomer form. **We choose $\hat{R}_{PA} = 2$, so that the steady state has roughly 75% in monomer form on the posterior. As shown in Fig. 6, this inhibition strength has little effect on the anterior, where pPARs are scarce. This matches experimental observations.**

2.3 The slow journey to a stable boundary position

We now try to understand how the boundary position is set. In Fig. 7, we simulate a maintenance phase “rescue” where the PAR-3 domain initially takes up 90% of the embryo. We use shading to show the dynamics up to time $\hat{t} = 500$ (50 minutes of real time). Initially, the boundary shifts because a high concentration of pPARs shifts the local equilibrium of PAR-3 oligomerization towards the monomer state, which makes bistability impossible [16]. Consequently, we observe contraction of the PAR-3 domain, with a peak that grows over time, and expansion of the PAR-2 domain, both of which eventually reach a steady state. The concentration of PAR-2 at the edge of the domain decreases over time, which suggests that cytoplasmic depletion might be responsible for halting the boundary, as there is at some point too much A and not enough P for P to win the competition (the decrease in P comes from both cytoplasmic depletion and cytoplasmic enrichment of CDC-42/PAR-6/PKC-3, which inhibit P). To demonstrate that the cytoplasmic dynamics are key to arresting posterior domain expansion, in the right panel of Fig. 7 we simulate with a cytoplasmic pool that is “frozen” at its value at $\hat{t} = 50$. The result is an anterior domain which shrinks at a constant rate with constant peak concentration, and a posterior domain which expands at a constant rate with the same concentration at the edge. If given enough time, the posterior domain would invade the entire embryo length.

What about the position of the boundary? Fig. 8 shows that the combination of cytoplasmic depletion and diffusion of PAR-3 monomers set a unique boundary position. Small amounts (10%) of initial PAR-3 enrichment lead to a different boundary position because PAR-3 assumes its intrinsic bistable state while the other proteins are distributed uniformly. Initial PAR-3 domain sizes 20% or larger lead to a single steady state boundary with about 50% PAR-3 enrichment and 25% PAR-2 enrichment. The rest of the domain is where the gradient of PKC-3 is set up.

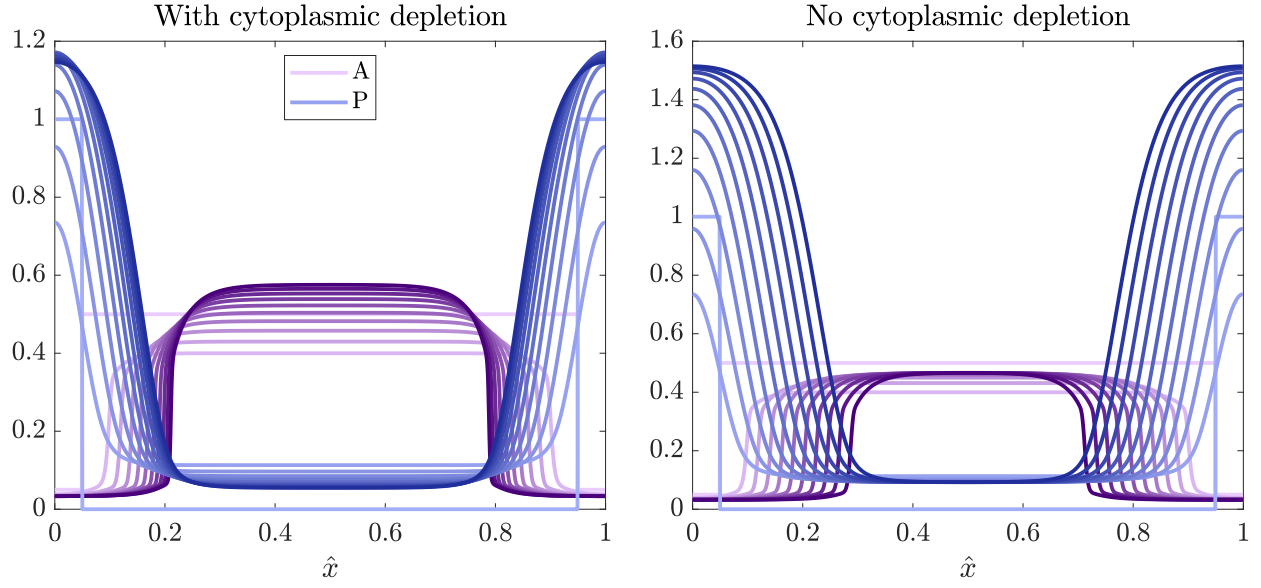


Figure 7: Simulating the biochemistry dynamics (14) with (left) and without (right) cytoplasmic depletion. We show a sequence of 11 time points from $\hat{t} = 0$ (the lightest colors) to $\hat{t} = 500$ (the darkest colors). The left plot shows results with the equations as written, while the right plot removes the cytoplasmic pool updates after $\hat{t} = 50$. For clarity of the plot, we show only PAR-3 in purple and pPARs in blue.

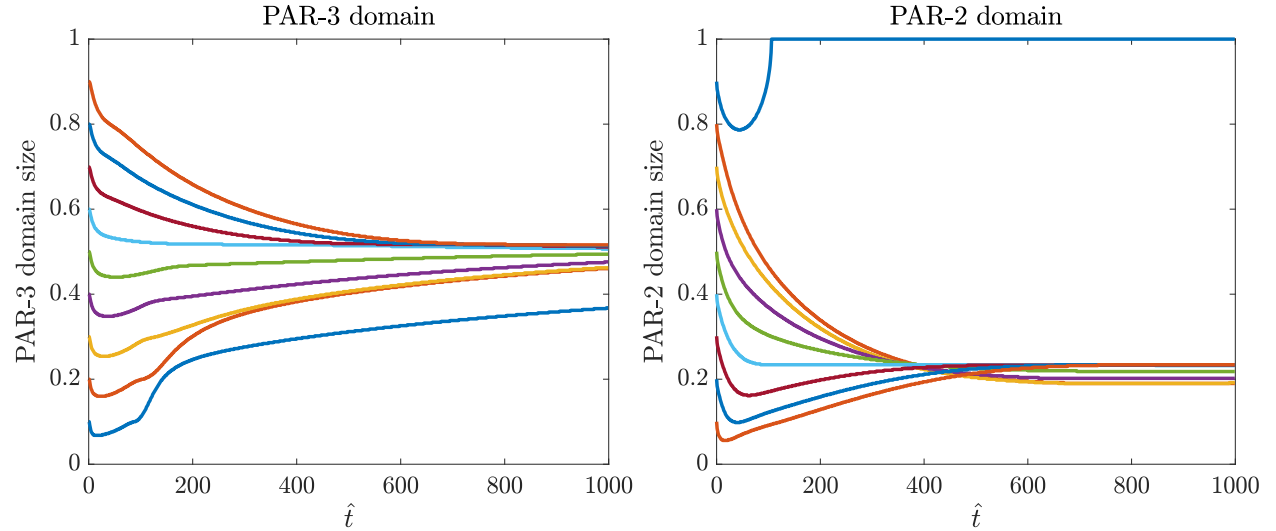


Figure 8: Size of the PAR-3 (left) and PAR-2 (right) domain over time for simulations of the model (14). Here the domain size is measured by the length of domain where a particular protein concentration is 80% of its maximum or larger.

If we begin with 90% PAR-3 enrichment, Fig. 8 shows that the PAR-3 domain size shrinks to roughly 80% after 5 minutes of real time. Considering that 5 minutes is the duration of maintenance phase, the process by which biochemistry amplifies asymmetries is intrinsically too slow to explain the maintenance-phase rescue process we see in live embryos. In the next section, we couple the contractility of Section 1 to biochemistry to speed up the rescue process.

3 Coupling contractility to biochemistry

Because myosin cannot form patterns on its own, there must be an interaction with PAR proteins that amplifies gradients in contractility to rescue the correct polarized state. To account for this, we add the myosin dynamics (1) to the biochemistry system (14). In doing this, we also incorporate advective terms that ensure that each protein moves with the local cortical velocity [13], and make CDC-42 a promoter of myosin by adding a term of the form $\hat{R}_{\text{CM}}\hat{C}\hat{M}_{\text{cyto}}$. In dimensionless form, the coupled system is

$$\partial_t \hat{A}_1 + \hat{\sigma}_0 \partial_{\hat{x}} (\hat{v} \hat{A}_1) = \hat{D}_A \partial_{\hat{x}}^2 \hat{A}_1 + \hat{K}_A^{\text{on}} \left(1 + \hat{K}_A^{\text{f}} \hat{F}_A(\hat{A})\right) \left(1 - \int_0^1 \hat{A}(x) d\hat{x}\right) - \hat{K}_A^{\text{off}} \hat{A}_1 \quad (18a)$$

$$+ 2\hat{A}_2 - 2\hat{K}_{\text{AP}}^{\text{p}} \hat{A}_1^2 + \sum_{n=3}^N \left(\hat{A}_n - \hat{K}_{\text{AP}}^{\text{p}} \hat{A}_1 \hat{A}_{n-1}\right)$$

$$\partial_t \hat{A}_n + \hat{\sigma}_0 \partial_{\hat{x}} (\hat{v} \hat{A}_n) = \hat{K}_{\text{AP}}^{\text{p}} \hat{A}_1 (\hat{A}_{n-1} - \hat{A}_n) - (\hat{A}_n - \hat{A}_{n+1}) \quad N > n \geq 2 \quad (18b)$$

$$\partial_t \hat{A}_N + \hat{\sigma}_0 \partial_{\hat{x}} (\hat{v} \hat{A}_N) = \hat{K}_{\text{AP}}^{\text{p}} \hat{A}_1 \hat{A}_{N-1} - \hat{A}_N \quad (18c)$$

$$\partial_t \hat{C} + \hat{\sigma}_0 \partial_{\hat{x}} (\hat{v} \hat{C}) = \hat{D}_C \partial_{\hat{x}}^2 \hat{C} + \hat{K}_C^{\text{on}} \left(1 - \int_0^1 \hat{C}(\hat{x}) d\hat{x}\right) - \hat{K}_C^{\text{off}} (1 + \hat{R}_{\text{PC}} \hat{P}) \hat{C} \quad (18d)$$

$$\partial_t \hat{K} + \hat{\sigma}_0 \partial_{\hat{x}} (\hat{v} \hat{K}) = \hat{D}_K \partial_{\hat{x}}^2 \hat{K} + \hat{R}_{\text{ACK}} \hat{C} \delta_{\hat{A} > \hat{A}_0} \left(1 - \int_0^1 \hat{K}(\hat{x}) d\hat{x}\right) - \hat{K}_K^{\text{off}} \hat{K} \quad (18e)$$

$$\partial_t \hat{P} + \hat{\sigma}_0 \partial_{\hat{x}} (\hat{v} \hat{P}) = \hat{D}_P \partial_{\hat{x}}^2 \hat{P} + \hat{K}_P^{\text{on}} \left(1 - \int_0^1 \hat{P}(\hat{x}) d\hat{x}\right) - \hat{K}_P^{\text{off}} (1 + \hat{R}_{\text{KP}} \hat{K}) \hat{P} \quad (18f)$$

$$\partial_t \hat{M} + \hat{\sigma}_0 \partial_{\hat{x}} (\hat{v} \hat{M}) = \hat{D}_M \partial_{\hat{x}}^2 \hat{M} + \hat{K}_M^{\text{on}} (1 + \hat{R}_{\text{CM}} \hat{C}) \left(1 - \int_0^1 \hat{M}(x) dx\right) - \hat{K}_M^{\text{off}} \hat{M} \quad (18g)$$

$$\hat{v} = \hat{\ell}^2 \partial_{\hat{x}}^2 \hat{v} + \hat{\ell} \partial_{\hat{x}} \hat{\sigma}_a(\hat{M}) \quad (18h)$$

$$R_{\text{CM}} = \frac{r_{\text{CM}} C^{(\text{Tot})}}{k_M^{\text{on}}}, \hat{K}_M^{\text{on}} = \frac{k_M^{\text{on}}}{h k_A^{\text{dp}}}, \hat{K}_M^{\text{off}} = \frac{k_M^{\text{off}}}{k_A^{\text{dp}}}, \hat{\sigma}_0 = \frac{\sigma_0 / \sqrt{\eta \gamma}}{L k_A^{\text{dp}}}, \hat{D}_M = \frac{D_M}{k_A^{\text{dp}} L^2}, \hat{\ell} = \frac{\sqrt{\eta / \gamma}}{L}. \quad (18i)$$

The last equation (18i) defines the key *new* dimensionless parameters relating to myosin. These differ from (6) because we can only non-dimensionalize time by one quantity, and we choose here to stick with the depolymerization time $1/k_A^{\text{dp}}$. Table 1 gives the dimensional quantities σ_0 , D_M ,

and k_M^{off} , from which we obtain $\hat{\sigma}_0$, \hat{D}_M , and \hat{K}_M^{off} . This leaves two parameters which control the myosin profile: the basal rate k_M^{on} , and the amount that CDC-42 promotes myosin, \hat{R}_{CM} . In wild-type and *arx-2* (RNAi) embryos, the minimum amount of bound myosin is 0.2. This sets k_M^{on} via $k_M^{\text{on}}/(k_M^{\text{on}} + k_M^{\text{off}}h) \approx 0.2$, giving $k_M^{\text{on}} = 0.3 \mu\text{m/s}$. Our task now is to see if there is a value of \hat{R}_{CM} which will reproduce maintenance phase rescue.

3.1 First attempt to simulate maintenance-phase rescue

We begin by simulating the model (18) (with parameters in Tables 1–3) with different choices of \hat{R}_{CM} . Two time sequences are shown in Fig. 9 ($\hat{R}_{\text{CM}} = 0.2$) and Fig. 10 ($\hat{R}_{\text{CM}} = 1$). In both cases, the initial dynamics are the same: an initially peaked profile of PAR-2 invades the anterior domain, concentrating anterior PARs in the middle and thereby increasing the concentration of pPARs in the posterior. As a result of this, CDC-42 gets inhibited in the posterior, which gives a gradient of myosin from posterior to anterior. The gradient of myosin generates a flow which further compacts the anterior domain.

The fundamental difference between Figs. 9 and 10 is the strength of the myosin gradient and the resulting flows. In Fig. 9, the rate at which CDC-42 promotes myosin is only 20% of the basal rate, and as a result the myosin gradient and resulting flow speeds are small. As a result, the boundary slowly contracts and is halted by cytoplasmic depletion of PAR-2 [9], similar to what we see without any flows at all. Figure 10 shows what happens when CDC-42 promotes myosin at 100% of the basal rate. There we see a strong myosin gradient and flow, which eventually focuses the PAR-3 domain into the center of the embryo. In the model, this peak will grow until it is balanced by diffusion (this is not shown in Fig. 10, because PAR-3 levels can reach $\hat{A} = 300$ when the peak keeps contracting).

Thus the model has identified two regimes of behavior, depending on the sensitivity of myosin to the CDC-42 concentration. Roughly speaking, if CDC-42 promotes myosin at a rate much smaller than the basal rate, the cytoplasmic dynamics are sufficient to stop the pPARs from invading too far into the anterior domain. But if CDC-42 promotes myosin at a rate comparable to the basal rate, the dynamics show a rapid concentration of the anterior domain into a peaked profile at the anterior pole. To further probe this behavior, in Fig. 11 we plot the size of the PAR-3 domain over time for four different values of \hat{R}_{CM} , including the case of $\hat{R}_{\text{CM}} = 0$, when there are no flows at all. We see again our two regimes of behavior: rescue can occur by slow diffusion of the boundary aided by flows, with an eventual steady state boundary position, or rapid flows can contract the

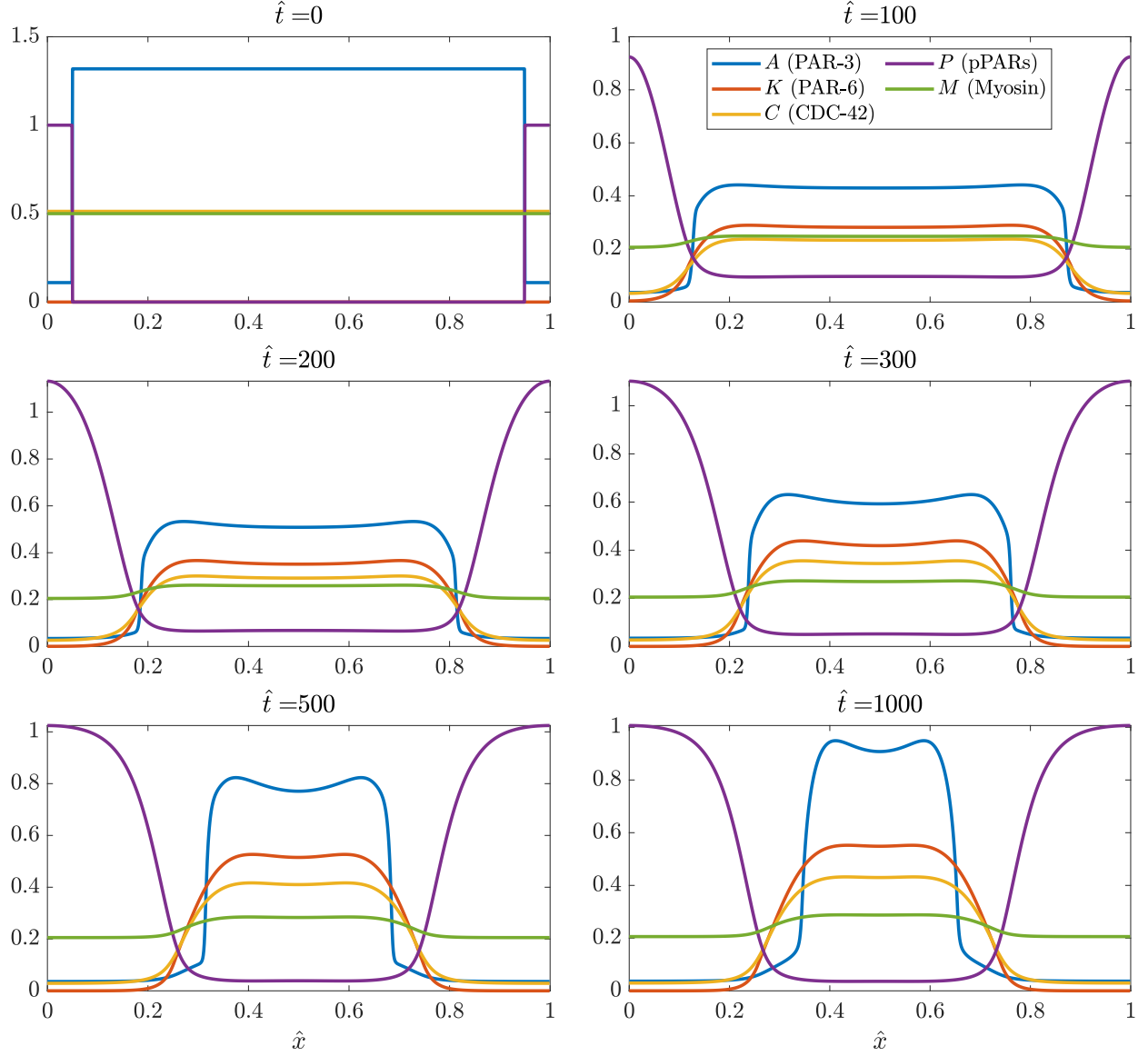


Figure 9: Time progression of an initially peaked profile of posterior PARs in the model (18) with $\hat{R}_{\text{CM}} = 0.2$. As shown at $\hat{t} = 0$ at top left, we begin with 10% depletion of PAR-3, then simulate the model (18) with the parameters in Tables 1–3.

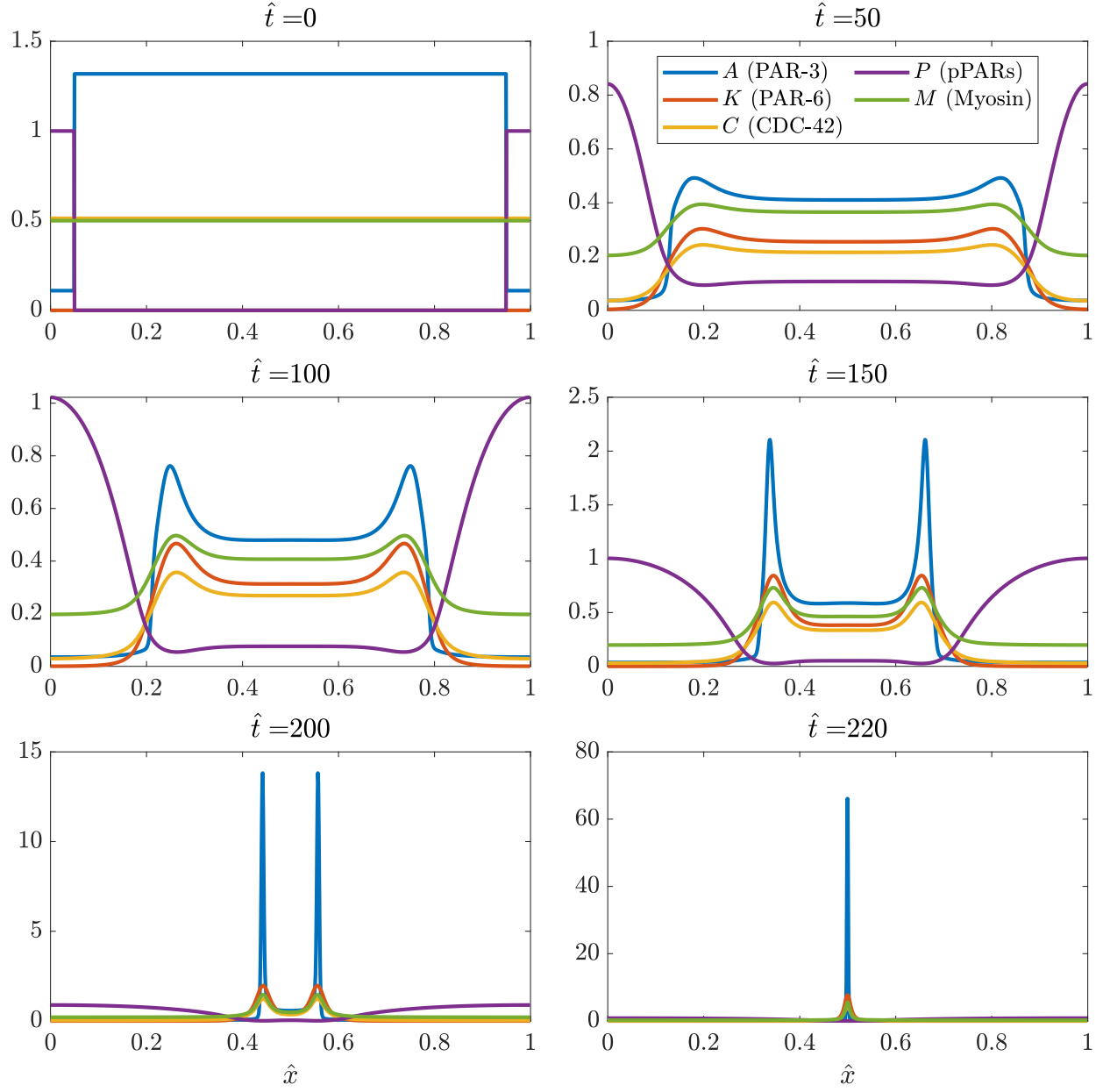


Figure 10: Time progression of an initially peaked profile of posterior PARs in the model (18) with $\hat{R}_{CM} = 1$.

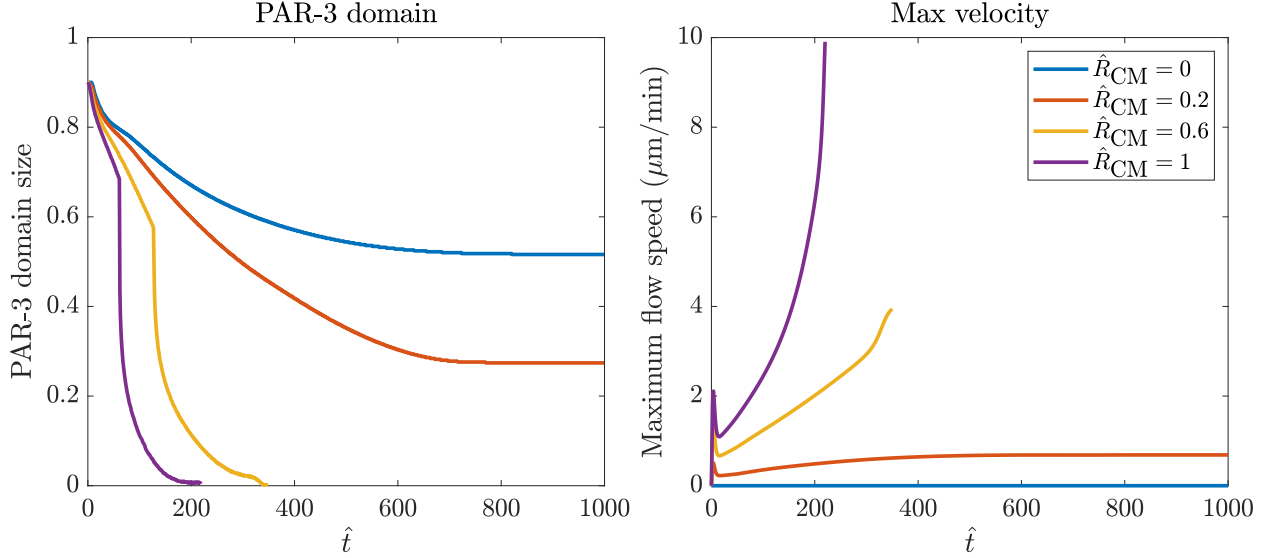


Figure 11: Simulations of rescue without branched actin. We repeat the simulation in Fig. 9 with a variety of values of \hat{R}_{CM} and plot the size of the PAR-3 domain over time (left) and the maximum cortical velocity over time (right).

anterior domain off the edge of the embryo.

The two regimes are most obvious when we look at the flow profiles in the right panel of Fig. 11: in the case when the boundary stops by cytoplasmic depletion (red lines), there is a slow increase in the velocity to a steady value. Alternatively, the velocity grows without bound when the domain contracts off the end of the embryo. Our problem is that neither of these two regimes is consistent with the data, where rescue of polarity occurs with an initially fast flow on the order 5–10 $\mu\text{m}/\text{min}$, followed by a slowing down of the flow and a settling to the steady state boundary position. Indeed, in embryos which lack *ect-2* and *nop-1* [28], maintenance-phase “rescue” of polarity occurs on timescales of a few minutes, and the aPAR domain goes from roughly 90% embryo length to 70% embryo length in a span of 160 seconds ($\hat{t} = 25.6$) [28, Fig. 7D]. We can replicate this behavior only if we set $\hat{R}_{CM} = 3$, in which case the PAR-3 domain contracts off the end of the embryo in ten minutes’ time. Thus, our model cannot predict a transition to a stable boundary with the flow speeds characteristic of maintenance-phase rescue.

3.2 Incorporating branched actin

The main issue with the models so far is that realistic flow speeds cause the anterior domain to contract off the end of the embryo. So, there must be some mechanism that could counteract the fast

Parameter	Description	Value	Units	Ref	Notes
D_R	Branched actin diffusivity	0.05	$\mu\text{m}^2/\text{s}$		Same as myosin
k_R^{off}	Branched actin unbinding rate	0.12	1/s		Same as myosin
\hat{R}_{CM}	C promoting M	3		[28, Fig. 7D]	Fit initial rescue speed
\hat{C}_R	Threshold CDC-42 level for branched actin	0.2			Between A and P levels
\hat{R}_{CR}	CDC-42 producing branched actin rate	1			Arbitrary
\hat{R}_{RM}	Branched actin inhibiting myosin rate	15			Fit boundary position

Table 4: Additional parameters for coupled model (18) with branched actin additions in (19).

flow speeds. Based on our experiments in *arx-2* (RNAi) embryos, which exhibit a hypercontractile state, it seems logical that branched actin could contribute to halting the progression of the anterior domain. Our hypothesis in particular is that branched actin is activated above a certain “threshold” of CDC-42, and that branched actin inhibits contractility by inhibiting myosin. We encode these properties in the system of equations by modifying the myosin equation in (18) and adding an additional equation for branched actin, which we represent by R ,

$$\begin{aligned}
\partial_t \hat{M} + \hat{\sigma}_0 \partial_x (\hat{v} \hat{M}) &= \hat{D}_M \partial_x^2 \hat{M} + \hat{K}_M^{\text{on}} (1 + \hat{R}_{\text{CM}} \hat{C}) \left(1 - \int_0^1 \hat{M}(x) dx\right) - \hat{K}_M^{\text{off}} (1 + \hat{R}_{\text{RM}} \hat{R}) \hat{M} \\
\partial_t \hat{R} + \hat{\sigma}_0 \partial_x (\hat{v} \hat{R}) &= \hat{D}_R \partial_x^2 \hat{R} + \hat{R}_{\text{CR}} (\hat{C} - \hat{C}_R) \delta_{\hat{C} > \hat{C}_R} \left(1 - \int_0^1 \hat{R}(x) dx\right) - \hat{K}_R^{\text{off}} \hat{R}
\end{aligned} \tag{19}$$

Here branched actin is produced above a threshold level \hat{C}_R of CDC-42, as indicated by the δ -function. Once produced, branched actin inhibits myosin. **We assume for the moment that branched actin has the same diffusivity ($0.05 \mu\text{m}^2/\text{s}$) and unbinding rate ($0.12/\text{s}$) as myosin.**

3.2.1 Additional parameters

There are four new parameters in this model that are unknown:

- \hat{R}_{CM} , which is the rate at which CDC-42 produces myosin. As mentioned in the last section, the value $\hat{R}_{\text{CM}} = 3$ gives a good match to the initial speeds of maintenance phase rescue reported in [28, Fig. 7D], which presumably do not yet have interference from branched actin.
- The threshold \hat{C}_R is set by examining the steady state in Fig. 9 without branched actin. There we see that, at late times, CDC-42 goes from about 0.05 in the posterior to 0.45 in the anterior. To block contractility, we set $\hat{C}_R = 0.2$.

- The rate at which CDC-42 produces branched actin sets the amount of bound branched actin. This amount is arbitrary, since what matters is not the amount of branched actin but the total amount of myosin inhibition. We therefore set $\hat{R}_{CR} = 1$.
- We set the rate at which branched actin blocks myosin $\hat{R}_{RM} = 10$, which is the parameter we use to control the dynamics, to reproduce the boundary position in wild type embryos.

The parameters are summarized in Table 4.

3.2.2 Dynamics

Figure 12 shows the dynamics of the approach to steady state for (18) augmented with the branched actin model (19). We see initially the same dynamics as in Fig. 10, with pPARs inhibiting CDC-42 and myosin, which produces an inward flow. However, once the CDC-42 concentration (yellow) gets high enough, branched actin (cyan) starts to be produced and inhibit contractility. This makes the myosin profile decrease, and stalls flow and movement of the boundary. The steady state is reached at about $\hat{t} = 100$, which corresponds to 10 minutes of real time (there is slow contraction of the boundary to its final resting place after this).

The advantage of incorporating branched actin is that we can essentially have arbitrarily fast initial flow speeds, which are later blocked by branched actin. As shown in Fig. 13, in our simulation there is initially a rapid build-up of flow and shrinking of the PAR-3 boundary. The flow then becomes smaller once branched actin kicks in, and both the flow speed and domain size plateau to a steady state. **These data for velocity over time qualitatively match what we see in experiments.**

There is still a role for cytoplasmic depletion in pinning the boundary. Without cytoplasmic depletion, a boundary that is moving will always keep moving, since the fundamental balance in which pPARs outcompete the aPARs does not change unless we account for changes in the cytoplasmic depletion. What branched actin allows for is a change in how the flow speed depends on the myosin concentration in time. Initially, when there is no branched actin, flows are fast. But, when branched actin is created, the flows slow down and the boundary can no longer rapidly contract, allowing it to be stalled by cytoplasmic depletion. Thus, branched actin *and* cytoplasmic depletion work together to stall the boundary at a point where the posterior PAR domain can no longer advance through the anterior PARs.

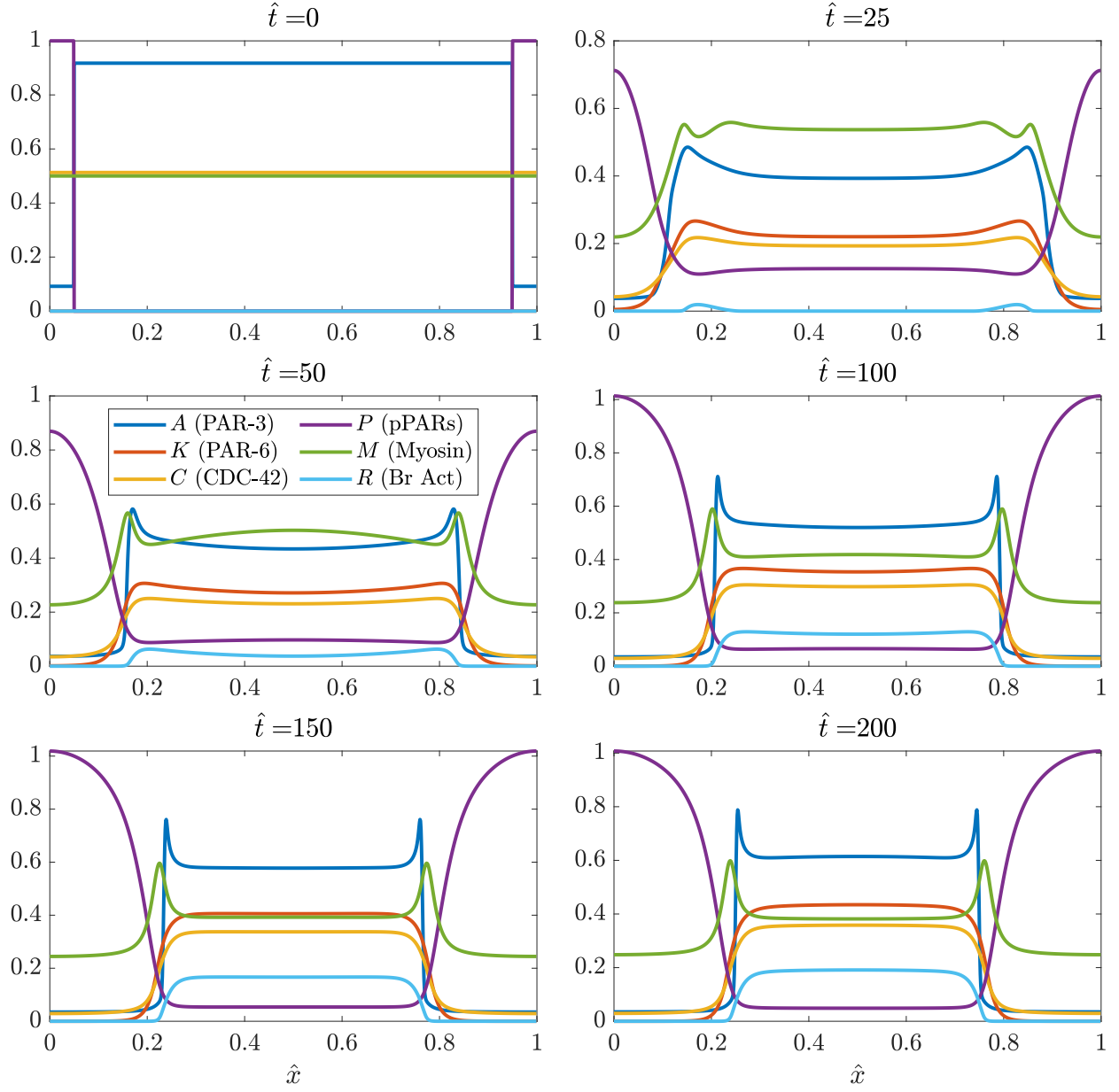


Figure 12: Simulation of maintenance phase rescue with branched actin. As shown at $\hat{t} = 0$ at the top left, we begin with 10% depletion of PAR-3, then simulate the model (18) *with branched actin* as in (19). The size of the aPAR domain initially shrinks rapidly, and then stalls as branched actin (cyan) starts to inhibit contractility.

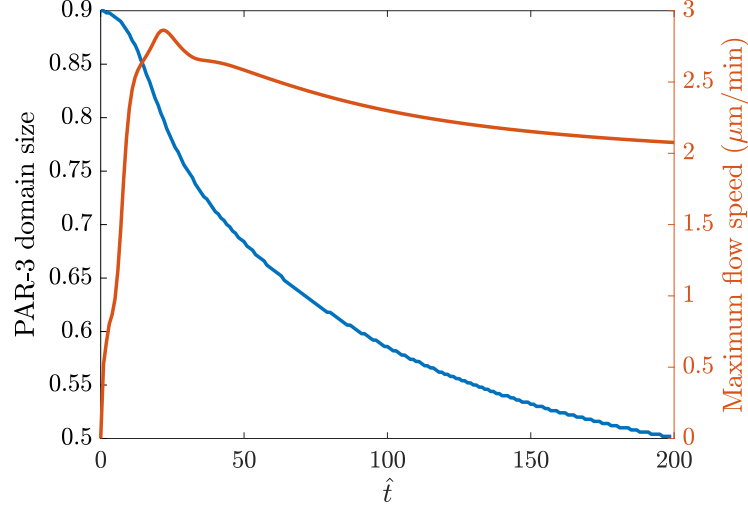


Figure 13: PAR-3 domain size and maximum flow speed in simulations maintenance-phase rescue. The initial conditions are as in the top left Fig. 12, with 90% of the domain enriched in PAR-3. The blue line (left axis) shows the boundary position over time, while the red line (right axis) shows the maximum flow velocity.

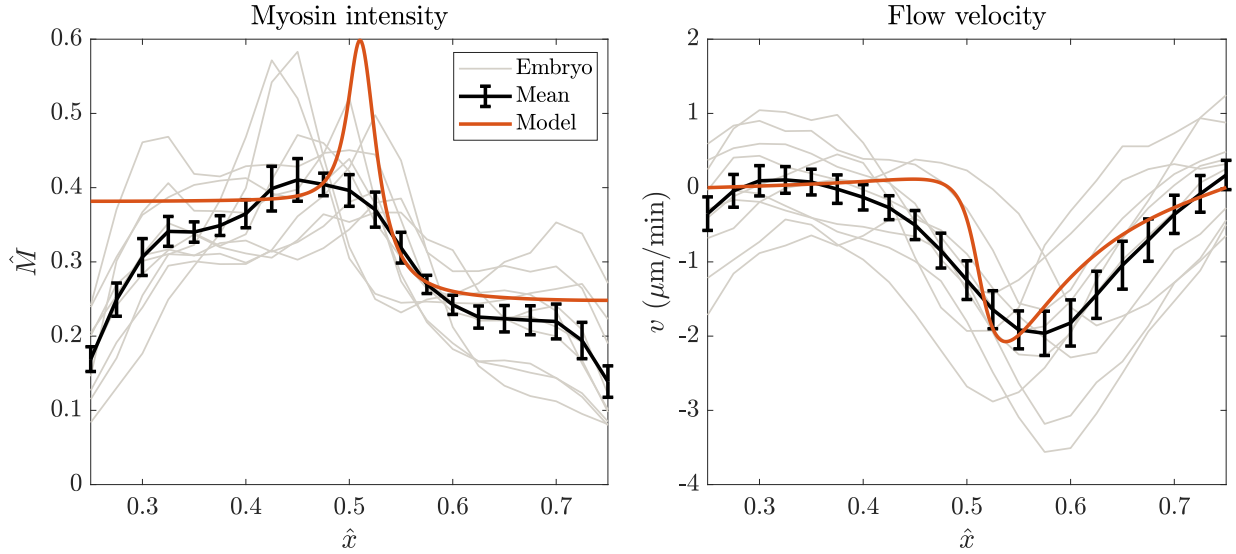


Figure 14: Steady state of the model (18) with branched actin model (19) (this corresponds to $\hat{t} = 200$ in the simulation of maintenance phase rescue depicted in Fig. 12), compared to experimental results for wild-type embryos. The left panel shows the myosin intensity profile, while the right panel shows the speed of flow. Individual embryos are shown using gray lines, the mean \pm standard error are shown in black. Results of the model (shifting the anterior pole to $\hat{x} = 0.25$) are overlaid in red.

3.2.3 Steady state vs. experiments

Figure 14 shows how our modeled steady state (after $\hat{t} = 200$ of maintenance phase rescue) compares to wild-type embryos (the “steady state” measured in late maintenance phase). Qualitatively, the results match: the myosin intensity displays a peak at the anterior cap, then drops off to a level midway between the peak anterior and posterior levels at the anterior pole. The flow also exhibits a maximum off of the anterior cap, then rapidly transitions to a stall point at the edge of the anterior domain.

Quantitatively, our results almost match up with the experiments, but leave a little to be desired. The issue is the lengthscale on which the drop in myosin occurs. Because branched actin is only active on the anterior cap, the lengthscale on which it goes from zero to its peak value is quite small (controlled by the diffusivity, which here is set equal to the diffusivity of myosin). As such, the myosin is inhibited quickly in the model, and the profile rapidly drops to a flat level in the anterior. This is *not* what is observed in experiments, where we see a more gradual decrease (although the individual embryos do show rapid decreases).

References

- [1] Alexander Beatty, Diane G Morton, and Kenneth Kemphues. Par-2, lgl-1 and the cdc-42 gap chin-1 act in distinct pathways to maintain polarity in the *c. elegans* embryo. *Development*, 140(9):2005–2014, 2013.
- [2] Justin S Bois, Frank Jülicher, and Stephan W Grill. Pattern formation in active fluids. *Biophysical Journal*, 100(3):445a, 2011.
- [3] Adrian A Cuenca, Aaron Schetter, Donato Aceto, Kenneth Kemphues, and Geraldine Seydoux. Polarization of the *c. elegans* zygote proceeds via distinct establishment and maintenance phases. 2003.
- [4] Adriana T Dawes and David Iron. Cortical geometry may influence placement of interface between par protein domains in early *caenorhabditis elegans* embryos. *Journal of theoretical biology*, 333:27–37, 2013.
- [5] Adriana T Dawes and Edwin M Munro. Par-3 oligomerization may provide an actin-independent mechanism to maintain distinct par protein domains in the early *caenorhabditis elegans* embryo. *Biophysical journal*, 101(6):1412–1422, 2011.

- [6] Evan B Dewey, Danielle T Taylor, and Christopher A Johnston. Cell fate decision making through oriented cell division. *Journal of developmental biology*, 3(4):129–157, 2015.
- [7] Wan Jun Gan and Fumio Motegi. Mechanochemical control of symmetry breaking in the *caenorhabditis elegans* zygote. *Frontiers in Cell and Developmental Biology*, 8:619869, 2021.
- [8] Raphaëla Geßele, Jacob Halatek, Laeschkir Würthner, and Erwin Frey. Geometric cues stabilise long-axis polarisation of par protein patterns in *c. elegans*. *Nature communications*, 11(1):539, 2020.
- [9] Nathan W Goehring, Philipp Khuc Trong, Justin S Bois, Debanjan Chowdhury, Ernesto M Nicola, Anthony A Hyman, and Stephan W Grill. Polarization of par proteins by advective triggering of a pattern-forming system. *Science*, 334(6059):1137–1141, 2011.
- [10] Bob Goldstein and Ian G Macara. The par proteins: fundamental players in animal cell polarization. *Developmental cell*, 13(5):609–622, 2007.
- [11] Peter Gross, K Vijay Kumar, Nathan W Goehring, Justin S Bois, Carsten Hoege, Frank Jülicher, and Stephan W Grill. Guiding self-organized pattern formation in cell polarity establishment. *Nature physics*, 15(3):293–300, 2019.
- [12] Niv Ierushalmi and Kinneret Keren. Cytoskeletal symmetry breaking in animal cells. *Current Opinion in Cell Biology*, 72:91–99, 2021.
- [13] Rukshala Illukkumbura, Nisha Hirani, Joana Borrego-Pinto, Tom Bland, KangBo Ng, Lars Hubatsch, Jessica McQuade, Robert G Endres, and Nathan W Goehring. Design principles for selective polarization of par proteins by cortical flows. *Journal of Cell Biology*, 222(8), 2023.
- [14] Kenneth J Kempf, James R Priess, Diane G Morton, and Niansheng Cheng. Identification of genes required for cytoplasmic localization in early *c. elegans* embryos. *Cell*, 52(3):311–320, 1988.
- [15] Natalia Kravtsova and Adriana T Dawes. Actomyosin regulation and symmetry breaking in a model of polarization in the early *caenorhabditis elegans* embryo: symmetry breaking in cell polarization. *Bulletin of mathematical biology*, 76:2426–2448, 2014.

- [16] Charles F Lang, Alexander Anneken, and Edwin Munro. Oligomerization and feedback on membrane recruitment stabilize par-3 asymmetries in *c. elegans* zygotes. *bioRxiv*, pages 2023–08, 2023.
- [17] Charles F Lang and Edwin Munro. The par proteins: from molecular circuits to dynamic self-stabilizing cell polarity. *Development*, 144(19):3405–3416, 2017.
- [18] Jean-Léon Maître, Hervé Turlier, Rukshala Illukkumbura, Björn Eismann, Ritsuya Niwayama, François Nédélec, and Takashi Hiragi. Asymmetric division of contractile domains couples cell positioning and fate specification. *Nature*, 536(7616):344–348, 2016.
- [19] Mirjam Mayer, Martin Depken, Justin S Bois, Frank Jülicher, and Stephan W Grill. Anisotropies in cortical tension reveal the physical basis of polarizing cortical flows. *Nature*, 467(7315):617–621, 2010.
- [20] Yoichiro Mori, Alexandra Jilkiné, and Leah Edelstein-Keshet. Wave-pinning and cell polarity from a bistable reaction-diffusion system. *Biophysical journal*, 94(9):3684–3697, 2008.
- [21] Edwin Munro, Jeremy Nance, and James R Priess. Cortical flows powered by asymmetrical contraction transport par proteins to establish and maintain anterior-posterior polarity in the early *c. elegans* embryo. *Developmental cell*, 7(3):413–424, 2004.
- [22] Masatoshi Nishikawa, Sundar Ram Naganathan, Frank Jülicher, and Stephan W Grill. Controlling contractile instabilities in the actomyosin cortex. *Elife*, 6:e19595, 2017.
- [23] François B Robin, William M McFadden, Baixue Yao, and Edwin M Munro. Single-molecule analysis of cell surface dynamics in *caenorhabditis elegans* embryos. *Nature methods*, 11(6):677–682, 2014.
- [24] Arnab Saha, Masatoshi Nishikawa, Martin Behrndt, Carl-Philipp Heisenberg, Frank Jülicher, and Stephan W Grill. Determining physical properties of the cell cortex. *Biophysical journal*, 110(6):1421–1429, 2016.
- [25] Anne Sailer, Alexander Anneken, Younan Li, Sam Lee, and Edwin Munro. Dynamic opposition of clustered proteins stabilizes cortical polarity in the *c. elegans* zygote. *Developmental cell*, 35(1):131–142, 2015.

- [26] Stephanie Schonegg and Anthony A Hyman. Cdc-42 and rho-1 coordinate acto-myosin contractility and par protein localization during polarity establishment in *c. elegans* embryos. 2006.
- [27] Filipe Tostevin and Martin Howard. Modeling the establishment of par protein polarity in the one-cell *c. elegans* embryo. *Biophysical journal*, 95(10):4512–4522, 2008.
- [28] Yu Chung Tse, Michael Werner, Katrina M Longhini, Jean-Claude Labbe, Bob Goldstein, and Michael Glotzer. Rhoa activation during polarization and cytokinesis of the early *caenorhabditis elegans* embryo is differentially dependent on *nop-1* and *cyk-4*. *Molecular biology of the cell*, 23(20):4020–4031, 2012.
- [29] Seth Zonies, Fumio Motegi, Yingsong Hao, and Geraldine Seydoux. Symmetry breaking and polarization of the *c. elegans* zygote by the polarity protein *par-2*. *Development*, 137(10):1669–1677, 2010.